PHYSICAL REVIEW B **82**, 174116 (2010)

Component-specific electromechanical response in a ferroelectric/dielectric superlattice

Ji Young Jo,[1] Rebecca J. Sichel,[1] Eric M. Dufresne,[2] Ho Nyung Lee,[3] Serge M. Nakhmanson,[4] and Paul G. Evans[1]
[1]*Department of Materials Science and Engineering and Materials Science Program, University of Wisconsin–Madison, Madison, Wisconsin 53706, USA*
[2]*Advanced Photon Source, Argonne National Laboratory, Argonne, Illinois 60439, USA*
[3]*Materials Science and Technology Division, Oak Ridge National Laboratory, Oak Ridge, Tennessee 37831, USA*
[4]*Materials Science Division, Argonne National Laboratory, Argonne, Illinois 60439, USA*

(Received 3 July 2010; revised manuscript received 8 September 2010; published 16 November 2010)

The electronic and electromechanical properties of complex oxide superlattices are closely linked to the evolution of the structure and electrical polarization of the component layers in applied electric fields. Efforts to deduce the responses of the individual components of the superlattice to applied fields have focused on theoretical approaches because of the limitations of available experimental techniques. Time-resolved x-ray microdiffraction provides a precise crystallographic probe of each component using the shift in wave vector and change in intensity of superlattice satellite reflections. We report in detail the methods to measure and analyze the x-ray diffraction patterns in applied electric field and their application to a 2-unit-cell $BaTiO_3$/4-unit-cell $CaTiO_3$ superlattice. We find that the overall piezoelectric distortion is shared between the two components. Theoretical predictions of the electromechanical properties of a superlattice with the same composition constrained to tetragonal symmetry are in excellent agreement with the experiments. Lattice instability analysis, however, suggests that the low-temperature ground state could exhibit antiferrodistortive rotations of TiO_6 octahedra within and/or at the interfaces of the $CaTiO_3$ component.

DOI: 10.1103/PhysRevB.82.174116 PACS number(s): 78.70.Ck, 77.80.bn, 77.80.bg

I. INTRODUCTION

Heteroepitaxial superlattices (SLs) of alternating ferroelectric (FE) and dielectric components with unit-cell-scale thicknesses exhibit a number of important phenomena arising from the introduction of a large static polarization into their dielectric constituent layers.[1,2] These phenomena include an enhancement of the dielectric permittivity,[3] control of the polarization direction by epitaxial strain engineering,[4] and formation of nanometer-scale stripe domain patterns.[5] Because the properties of SLs can be dramatically different from those of bulk materials with the same average chemical composition,[6] such heterostructures hold great promise for the design of materials with enhanced or even completely unexpected functionalities. The integration of SLs into electrical device structures allows these materials to be driven far from equilibrium, both electrically and mechanically, by electric fields on the order of 1 MV/cm.[7] As we show in this paper, theoretical and experimental methods now allow the functional properties of SLs under these conditions to be predicted and probed with atomic-scale precision.

Here we describe in detail the nonequilibrium properties of a model SL with a repeating unit consisting of 2 unit cells of $BaTiO_3$ and 4 unit cells of $CaTiO_3$, $2(BaTiO_3)/4(CaTiO_3)$. Based on experimental results from dielectric/ferroelectric SLs of similar composition and on electrostatic arguments,[8–13] we intuitively expect that the $CaTiO_3$ layers of the $BaTiO_3/CaTiO_3$ SL will be electrically polarized with approximately the same polarization as the $BaTiO_3$ layers. As we show below, these intuitive arguments agree with a complete first-principles calculation. The polarization of the SL provides insight into its electromechanical properties because in mean-field theories of ferroelectricity the piezoelectric coefficients are proportional to the product of the remnant polarization, the dielectric constant, and the electrostrictive coefficient.[14] With the simplifying assumption that the latter two quantities have bulk values, we can thus expect that both the SL as a whole and its individual component layers exhibit piezoelectricity. We also show below that quantitative electromechanical predictions derived from first-principles theory are consistent with the expectations based on mean-field theory.

Previous studies have probed the structure of SLs in the absence of externally applied electric fields. Electron microscopy studies, for example, have shown that the zero-electric-field structure of a $BaTiO_3/SrTiO_3$ SL has tetragonal distortion consistent with density-functional theory (DFT) predictions, thus providing evidence for the polarization of the dielectric layers.[1] Similar agreement with the predicted ground-state structure has been obtained in measurements of the ferroelectric Curie temperatures of $PbTiO_3/SrTiO_3$ SLs.[15] To date, studies of SLs have not probed the evolution of individual component layers under applied electric fields or the connection between field-induced changes in their structure and electromechanical and dielectric properties.

The response of SLs to external fields such as mechanical stress (σ) and electric field (E) yields changes in the polarization (P) and strain (ε) that are defined by the elastic, dielectric, and piezoelectric constants. Piezoelectricity is the linear relationship between the mechanical quantities ε and σ, and the electrical quantities E, and P, as illustrated in Fig. 1.[16,17] The relationships shown in Fig. 1 have previously been probed experimentally in SLs at the level of the average of the ferroelectric, dielectric, and electromechanical properties across the entire thickness of the SL.[17,18] Experimental probes of the atomic-scale structural effects arising from the piezoelectricity of individual components have confronted the difficulty of performing *in situ* structural measurements in applied electric fields. As a result, it has been difficult to

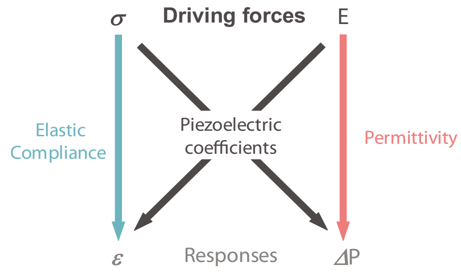

FIG. 1. (Color online) Relationships between polarization P, electric field E, stress σ, and strain ε.

test theoretical predictions of the functional properties of SLs.

We have used *in situ* x-ray diffraction and DFT calculations to study the structural origin of the electromechanical properties of a $2(BaTiO_3)/4(CaTiO_3)$ ferroelectric/dielectric SL. A $BaTiO_3/CaTiO_3$ SL was chosen for these studies because this composition is predicted to possess a large remnant polarization in both layers.[19] We have already reported that the $BaTiO_3/CaTiO_3$ SL as a whole has a piezoelectric coefficient d_{33} of 54 pm/V and that the $CaTiO_3$ component contributes to the piezoelectricity of the SL.[20] Here we present further experimental and theoretical results. The remainder of the paper is organized as follows: Sec. II is devoted to technical details of both experimental and theoretical methods. In Secs. III A and III B, we describe both steady-state and *in situ* E-dependent superlattice x-ray diffraction experiments and the analysis methods developed to resolve the electromechanical responses of each component of the SL. In Sec. III C, we present theoretical results, including predictions of piezoelectric coefficients of $BaTiO_3/CaTiO_3$ SLs, an explanation of the role of the $CaTiO_3$ component in the piezoelectricity of the SL, and predictions of unstable phonon modes in a SL constrained to tetragonal symmetry. The conclusions are summarized in Sec. IV.

II. EXPERIMENTAL AND THEORETICAL METHODS

A. Experimental methods

The SL was deposited by pulsed laser deposition onto a 4-nm-thick $SrRuO_3$ conducting bottom electrode on an (001)-oriented $SrTiO_3$ substrate.[7] The overall structure consisted of 80 periods of a repeating unit of 2 unit cells of $BaTiO_3$ and 4 unit cells of $CaTiO_3$, so that the nominal total thickness was 200 nm. An x-ray reciprocal space map around a $SrTiO_3$ {103} reflection using a laboratory x-ray diffractometer showed that the in-plane lattice constant of the SL was identical to that of $SrTiO_3$ substrate and that the as-grown SL is thus epitaxially clamped to the substrate. Capacitors were fabricated by depositing Pt top electrodes with a diameter of 100 μm. A remnant polarization of 0.1 C/m^2 was observed in polarization-electric field hysteresis loops.[21] We attribute the difference between the electrically observed polarization and the far larger predicted value given below either to the decomposition to the superlattice into domains at zero electric field or to a structural instability in the $CaTiO_3$ layers, discussed in detail in Sec. III C. Based on the prior theoretical results introduced in Sec. I,[8–12] the $CaTiO_3$ layer can be expected to possess the same remnant polarization as that of the $BaTiO_3$ layer.

Diffraction patterns of the SL in an applied electric field were acquired in time-resolved x-ray microdiffraction experiments conducted at station 7-ID of the Advanced Photon Source (APS). X rays with a photon energy of 10 keV were focused by a Fresnel zone plate to a 300 nm spot within the area in which the SL was covered by a top electrode.[22] An order-sorting aperture eliminated radiation that was not focused to the first order of the zone plate. The intensity of the diffracted beam was recorded using an avalanche photodiode detector. The detection electronics were configured to accumulate a maximum of one count for each synchrotron x-ray pulse, which arrived at a rate of 6.5 MHz in the 24-bunch operating mode of the APS. For relatively strong reflections, a series of attenuators was thus used to reduce the photon flux to the detector to below 10^6 counts/s in order to reduce the likelihood that the detector receives two x-ray photons during a single pulse.

The top electrode of the capacitor was contacted using a tungsten probe tip connected to a function generator. The applied E consisted of a triangular waveform with a duration of 2.5 ms, reaching a maximum field of 1.25 MV/cm. A multichannel scaler (MCS) was synchronized to the applied E with a total scan time of 5 ms, capturing a duration of 1.25 ms before and after the applied field. The MCS counted diffracted x-ray photons in 500 channels with a dwell time of 10 μs per channel.[23] By repeating the time-resolved diffraction measurement at a series of diffraction angles, we obtained a map of diffracted intensity as a function of counting channel and scattering wave vector.

To achieve sufficiently accurate intensity measurements for the subsequent analysis, the intensities recorded in the MCS channels were accumulated during a large number of cycles of E. The count rate at the peak of most intense SL reflection near the $SrTiO_3$ (002) reflection, attenuated as described above, was 6×10^5 counts/s, resulting in approximately 6 counts per channel during a single cycle of the electric field. The applied E was thus repeated until the sum of the intensities in each channel reached several hundred counts, which allowed us to achieve statistical uncertainties of approximately 5%. Depending on the intensity of the SL reflection, data acquisition required between 80 and 2000 repetitions of the E waveform.

B. First-principles calculation methods

A plane-wave DFT method[24] with ultrasoft pseudopotentials[25] was used to study the electronic, structural, and vibrational properties of the SL. The local-density approximation accounted for exchange and correlations. The electronic wave function and density plane-wave cutoffs were 30 and 300 Ry, respectively. During the structural relaxation, the symmetry of the tetragonal $1 \times 1 \times 6$ unit-cell supercell was restricted to space group $P4mm$ (point group C_{4v}) with a $6 \times 6 \times 1$ Monkhorst-Pack (MP) mesh being employed for the integrations in the tetragonal Brillouin zone

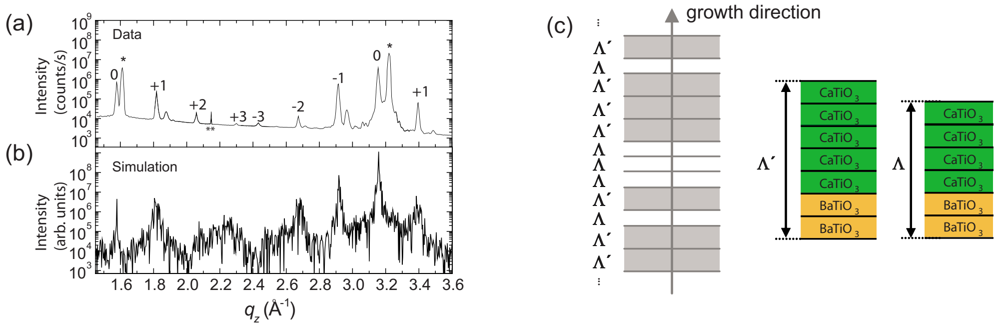

FIG. 2. (Color online) (a) Experimental diffraction pattern for the $2(BaTiO_3)/4(CaTiO_3)$ SL. Reflections are apparent at indices $l=0, +1, +2$, and $+3$ with $m=1$ and at $l=-3, -2, -1, 0$, and $+1$ with $m=2$. The symbols indicate (*) the (001) and (002) reflections from $SrTiO_3$ substrate and (**) an artifact associated with the reflection of third-harmonic radiation produced by the undulator insertion device from $SrTiO_3$ (004) planes. The $m=2$ $l=0$ and substrate (001) and (002) reflections were acquired with an x-ray attenuator placed before the sample and have been corrected in this plot. (b) Kinematic simulation of the diffraction pattern of a SL with a random variation in the number of layers in each repeating unit, as schematically displayed in (c). (c) Diagram of the random sequence of repeating units, each containing either 4 or 5 $CaTiO_3$ unit cells, labeled Λ and Λ', respectively. Both Λ and Λ' repeating units contain 2 $BaTiO_3$ unit cells. This structure yields a SL in which the average number of atomic layers in the repeating unit along the growth direction z is not an integer.

(BZ).[26] We discuss the structural symmetry of this SL in more detail in Sec. III C. The in-plane lattice constant, a, was constrained to the simulated equilibrium lattice constant of the cubic $SrTiO_3$ substrate (3.851 Å in this investigation) and the out-of-plane lattice constant c was allowed to vary. The system was considered to be at equilibrium when the forces on the ions were less than 0.01 eV/Å and the σ_3 (out of plane) component of the stress tensor was smaller than 0.2 kbar.

A density-functional perturbation theory approach[27] was used to obtain the ionic Born effective charges and to compute phonon band dispersions throughout the tetragonal BZ. The Berry-phase method was used to estimate the total polarization of the SL and evaluate its piezoelectric properties.[28] The $6\times6\times4$ MP mesh used in the Berry-phase calculations produced well-converged results.

The out-of-plane polarization profile for the SL was computed by decomposing the total supercell polarization into contributions from individual primitive cells. The polarization contribution P_λ from cell λ was estimated using the linearized approximation

$$P_\lambda \cong \sum_i \frac{\partial P}{\partial u_{\lambda i}^{(0)}}\left(u_{\lambda i}-u_{\lambda i}^{(0)}\right) = \frac{1}{V_\lambda}\sum_i Z^*_{\lambda i}\cdot \Delta u_{\lambda i}, \qquad (1)$$

where $Z^*_{\lambda i}$ and $\Delta u_{\lambda i}$ are the Born effective charge and displacement of the ith ion in the λth cell, and V_λ is the volume of the cell containing the A-site ions in the corners. The polarization, ionic displacements, and components of the Born-effective-charge tensor were constrained to the [001] direction. A superscript zero refers to a nonpolar structure with ferroelectric displacement removed by unbuckling the AO and BO_2 planes and moving the TiO_2 planes to the center of each primitive cell.

In the linear regime, the polarization changes ΔP_α due to changes σ in stress or ε in strain are connected via the piezoelectric tensors d and e, respectively (as schematically shown in Fig. 1). The same tensors also connect σ and ε with the applied field E. In Voigt notation these relationships are[16]

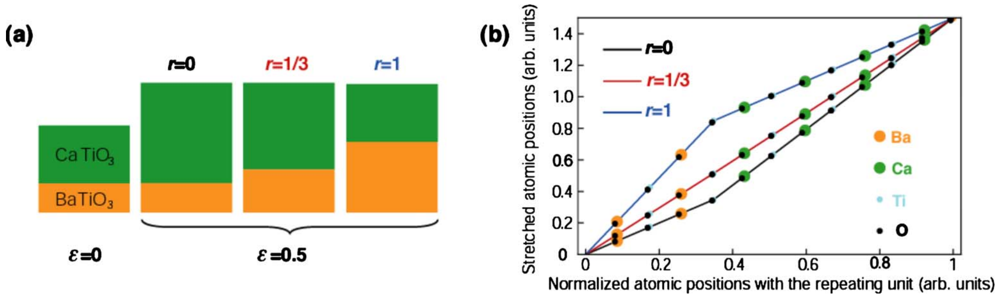

FIG. 3. (Color online) (a) Schematic of the distribution of the total piezoelectric distortion between $BaTiO_3$ and $CaTiO_3$ components of the SL for different values of the parameter r, illustrated for the hypothetical case of an unphysically large strain of $\varepsilon=50\%$. (b) Positions of atoms relative to the overall unit cell for $\varepsilon=50\%$, generated by distorting the structure obtained in DFT calculations with $\varepsilon=0$. Positions are plotted for the cases in which the piezoelectric strain occurs only in the $CaTiO_3$ layers ($r=0$), only in the $BaTiO_3$ layer ($r=1$), and for equal piezoelectric strains in both layers ($r=1/3$).

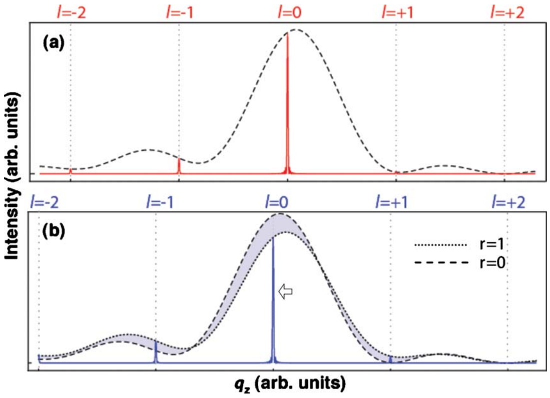

FIG. 4. (Color online) Kinematic x-ray diffraction simulation of the square of the structure factor, $|F|^2$, for the $2(\mathrm{BaTiO_3})/4(\mathrm{CaTiO_3})$ SL with (a) $\varepsilon=0$ and (b) $\varepsilon=1\%$. The arrow in (b) indicates the shift of the reflections to lower q_z due to piezoelectric expansion. The dashed and solid black lines are predictions for the $r=0$ and $r=1$ cases, respectively. The series of sharp peaks labeled with the values of l illustrate how the periodicity of the SL results in Bragg reflections for which the intensity is set by $|F|^2$.

$$\Delta P_\alpha=\sum_\beta d_{\alpha\beta}\sigma_\beta=\sum_\beta e_{\alpha\beta}\varepsilon_\beta, \quad \varepsilon_\alpha=\sum_\beta d_{\alpha\beta}E_\beta,$$

$$\sigma_\alpha=-\sum_\beta e_{\alpha\beta}E_\beta. \tag{2}$$

With the assumption of $P4mm$ symmetry, the SL has only two independent piezoelectric coefficients connected to the polarization change in the [001] direction: d_{31}, which is equal to d_{32}, and d_{33}.[16] The same relationships among components apply to $e_{\alpha\beta}$.

Epitaxial clamping of the SL to the substrate induces a fixed in-plane biaxial strain. As a result, the strains along [100] and [010], ε_1 and ε_2 respectively, are equal and constant. The out-of-plane stress σ_3 is set to zero to simulate the elastic relaxation of the SL along the growth direction. These boundary conditions result in a set of clamped, or apparent, piezoelectric coefficients with values that are different from their unclamped counterparts.[29] For the clamped system, $\Delta P_3=e_{33}\varepsilon_3$ when expressed using $e_{\alpha\beta}$, and $\Delta P_3=2d_{31}\sigma_1+d_{33}\sigma_3$ when expressed using $d_{\alpha\beta}$. Here, $\varepsilon_3=(c-c_0)/c_0$ is the strain along [001] in the clamped SL, with c_0 defined as the out-of-plane lattice parameter under no applied field E. The clamped e_{33} is then $[P_3^{(s)}-P_3^{(u)}]/\varepsilon_3$, where $P_3^{(s)}$ and $P_3^{(u)}$ are the polarizations in the strained and unstrained clamped states of the SL. Clamped piezoelectric coefficients d_{31} and d_{33} can be obtained by distorting the supercell to induce strain ε_3, computing the resulting changes in polarization P_3 and stresses σ_1 and σ_3, and then solving the system of linear equations in Eq. (2).

The experimental and computational results reported in Sec. III were obtained using two different forms of the piezoelectric effect. In the experiment, the converse piezoelectric coefficients were determined by measuring the lattice strain ε induced by an applied field E while in the computational study, the direct piezoelectric coefficients were acquired by computing the change in polarization corresponding to an applied stress σ. In the absence of nonlinearities, the piezoelectric coefficients $d_{\alpha\beta}$ produced by both effects are exactly equal.[16] It is also possible to obtain the piezoelectric coefficients by directly applying a static homogeneous electric field to the system (i.e., utilizing the converse effect). Such calculations, however, are more challenging than those using the direct piezoelectric effect approach and can also cause dielectric breakdown due to interband or Zener charge leakage in higher applied fields.[30]

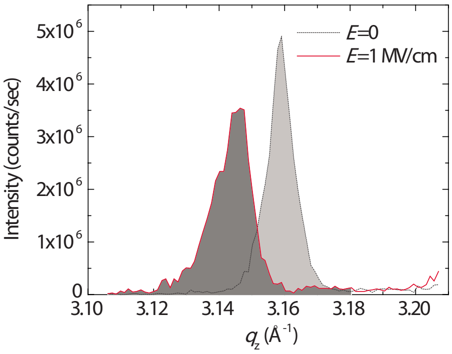

FIG. 5. (Color online) The $l=0$ $m=2$ SL x-ray reflection at zero electric field (light shading) and at $E=1$ MV/cm (dark shading).

III. PIEZOELECTRIC RESPONSES OF THE SUPERLATTICE

A. Steady-state ($E=0$) x-ray diffraction pattern of the superlattice

Along the [001] direction of reciprocal space, the x-ray diffraction pattern of the SL consists of a series of satellite reflections. These reflections appear with values of the [001] component of scattering wavevector, q_z, given by

$$q_z=\frac{2\pi}{t_{\mathrm{avg}}}\left(m+\frac{l}{n}\right). \tag{3}$$

Here n is the total number of atomic layers in the repeating unit and t_{avg} is the average lattice constant.[31] Each SL reflection is labeled with m and l, where m is an integer greater than or equal to zero and l can be any integer. The experimental diffraction pattern shown in Fig. 2(a) was acquired over a wide range of q_z using the synchrotron x-ray microdiffraction approach with $E=0$.

The experimentally observed average separation between adjacent reflections along q_z, corresponding to $\Delta l=\pm 1$, is $0.24\ \text{Å}^{-1}$. With the value of t_{avg} obtained from the $l=0$ reflections, 3.98 Å, the separation of adjacent superlattice reflections corresponds to $\Delta q_z=2\pi/6.6t_{\mathrm{avg}}$, giving $n=6.6$. This noninteger value of n arises from the presence of random variations in the thickness of the repeating unit during the deposition of the SL.[31] A similar effect has been reported in the diffraction patterns of semiconductor heterostructures.[32] The variation in layer thickness can occur in the number of atomic layers in the $\mathrm{BaTiO_3}$ or $\mathrm{CaTiO_3}$ components, or in a combination of both. Figure 2(b) shows a simulated diffraction pattern with the arbitrary assumption that all of the variation occurs in $\mathrm{CaTiO_3}$. Under this assumption, a random

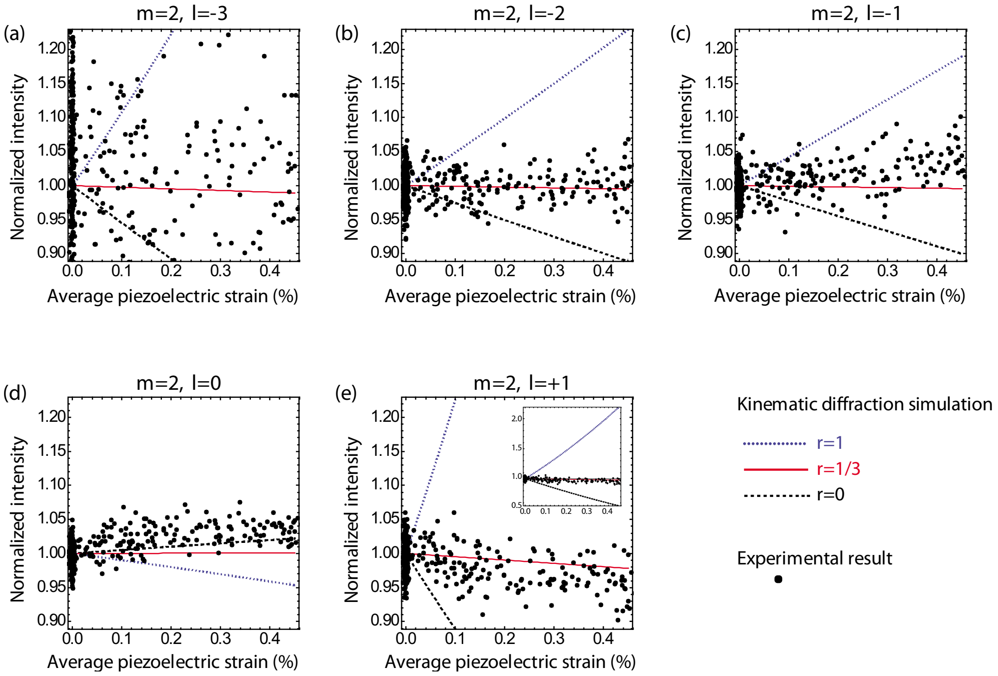

FIG. 6. (Color online) Variation in the experimentally observed integrated intensity of satellite reflections at $m=2$ and (a) $l=-3$, (b) $l=-2$, (c) $l=-1$, (d) $l=0$, and (e) $l=+1$ as a function of strain ε. The intensity of each reflection is plotted as the ratio of the observed intensity to the intensity at $\varepsilon=0$. The inset in (e) shows the predicted and observed intensities of $m=2$ $l=+1$ reflection plotted over an expanded range.

sequence of repeating units each containing either 4 or 5 $CaTiO_3$ unit cells is stacked to assemble the SL. The repeating units of different thicknesses are labeled Λ and Λ' respectively in the schematic in Fig. 2(c). The structure in Fig. 2(c) yields a SL in which the average number of atomic layers in each repeating unit is 6.6, producing satellite reflections at the q_z values matching the experimental data in Fig. 2(a). The weak reflections at $q_z=2.96$ and 3.485 Å^{-1} correspond to the $m=2$ $l=-1$ and $m=2$ $l=+1$ reflections of SLs with repeating units consisting of 2 $BaTiO_3$ and 4 $CaTiO_3$ unit cells. The intensities of these peaks a factor of 20 smaller than the peaks labeled $l=-1$ and $m=2$ $l=+1$ in Fig. 2(a). The weak reflections arise from a small fraction of the sample, and because they are thus not representative of the sample as a whole, we have not used them for further analysis.

B. Experimental probes for component-specific electromechanical responses

In order to analyze the structural changes accompanying the piezoelectric distortion of the SL, experimental diffraction patterns were compared with the results of a kinematic diffraction simulation. To simplify the analysis, the diffraction simulation used the ideal period $6t_{\text{avg}}$, with 2 unit cells of $BaTiO_3$ and 4 unit cells of $CaTiO_3$. In order to decompose the total piezoelectric strain into contributions from the individual components, we define a parameter r, which is the fraction of the total piezoelectric displacement occurring the $BaTiO_3$ component.[20] When $r=n_{BaTiO_3}/n$ or $r=1/3$ in the $2(BaTiO_3)/4(CaTiO_3)$ SL, both components have equal piezoelectric distortion, where n_{BaTiO_3} and n_{CaTiO_3} represent the number of atomic layers in the $BaTiO_3$ and $CaTiO_3$ compo-

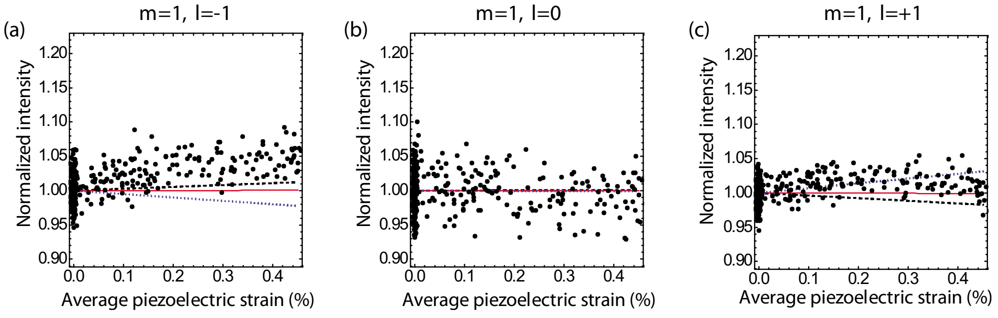

FIG. 7. (Color online) Variation in the intensity of satellite reflections at $m=1$ and (a) $l=-1$, (b) $l=0$, and (c) $l=+1$. The intensity of each reflection is plotted as the ratio of the observed intensity to the intensity at $\varepsilon=0$.

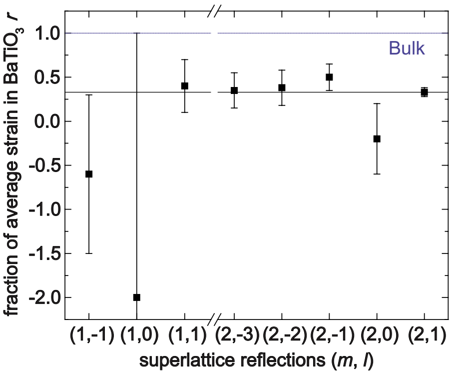

FIG. 8. (Color online) The fraction r of the average piezoelectric strain occurring in the $BaTiO_3$ component of the $2(BaTiO_3)/4(CaTiO_3)$ SL, obtained from experimental results in Figs. 6 and 7. The line labeled Bulk indicates the $r=1$ case, in which only $BaTiO_3$ component contributes to the piezoelectricity. Experimental results are close to line indicating the $r=1/3$ case, in which the piezoelectric distortions of $BaTiO_3$ and $CaTiO_3$ are equal.

nents, respectively. The definition of r is illustrated in Fig. 3(a).

The atomic positions used to simulate the diffraction pattern of the piezoelectrically expanded SL structure were produced by stretching the relaxed atomic structure obtained in DFT calculations. The scaled atomic positions that result from applying this model with different values of r are shown in Fig. 3(b), illustrated with a hypothetical very large ε of 50%. Figure 3(b) shows three cases: (1) $r=0$, in which the strain results from only $CaTiO_3$, (2) $r=1/3$, with the strain equally arising in both $CaTiO_3$ and $BaTiO_3$, and (3) $r=1$, with strain only in $BaTiO_3$, as would be expected from materials with their bulk properties.

The structure factor F of the repeating unit of the SL is the sum over all atoms j of $f_j \exp(i\mathbf{q}\cdot\mathbf{r_j})$.[33] Here $\mathbf{q}$ is the scattering wave vector and f_j and $\mathbf{r_j}$ are the atomic form factor and position of the jth atom. Atomic form factors are taken from Ref. 34. The scattered x-ray intensity from the SL as a whole is proportional to the square magnitude of the structure factor, $|F|^2$. Figure 4 shows plots of $|F|^2$ for the $2(BaTiO_3)/4(CaTiO_3)$ SL with (a) $E=0$ and (b) $E\neq 0$ and a piezoelectric distortion of 1%. The F of the piezoelectrically strained SL in Fig. 4(b) depends on the contributions of each component to the average piezoelectric strain ε, and is thus a function of r. Solid lines in Fig. 4 correspond to the normalized intensity of the SL diffraction pattern, which effectively samples the F of the repeating unit at each q_z value. The distortion of the lattice shifts all SL reflections to lower q_z, as the arrow indicates in Fig. 4(b). The kinematic diffraction simulation shows that the intensity of the SL reflections can be expected to change during piezoelectric expansion, and that the magnitude of the change depends on the value of r. This effect is illustrated for the two extreme cases $r=0$ and $r=1$ in Fig. 4(b).

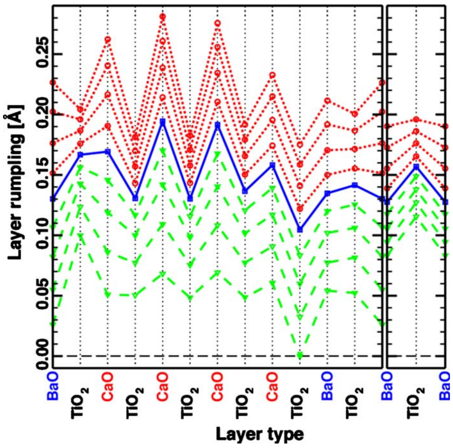

FIG. 9. (Color online) Layer rumplings in the $2(BaTiO_3)/4(CaTiO_3)$ SL for $\varepsilon_3=0\%$ (squares) and for axial tensions (circles), and compressions (triangles) of up to 2% in 0.5% steps. For comparison, the same data are also shown in the panel on the right for the $BaTiO_3$ thin film clamped to the $SrTiO_3$ substrate.

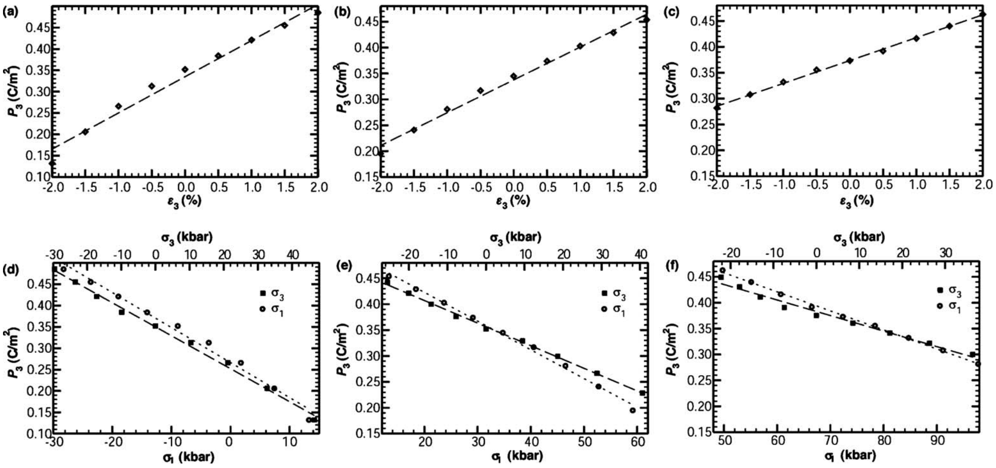

FIG. 10. Calculated dependence of P_3 on ε_3 for (a) the experimentally probed $2(BaTiO_3)/4(CaTiO_3)$ SL, (b) the $4(BaTiO_3)/2(CaTiO_3)$ SL, and (c) the clamped $BaTiO_3$ thin film. $P_3(\sigma_1)$ (open circles) and $P_3(\sigma_3)$ (solid squares) dependencies for (d) the experimentally probed $2(BaTiO_3)/4(CaTiO_3)$ SL, (e) the $4(BaTiO_3)/2(CaTiO_3)$ SL, and (f) the clamped $BaTiO_3$ thin film. The lines show the linear fits to the results that are used to extract the predicted piezoelectric coefficients.

The individual contributions of $BaTiO_3$ and $CaTiO_3$ to the piezoelectric strain can be resolved by analyzing the experimental variation in the intensities of the satellite reflections as a function of ε. When the strains in each component are equal, as with $r=1/3$ for the $2(BaTiO_3)/4(CaTiO_3)$ SL, the relative positions of the atomic planes are approximately the same within the elongated structural unit, resulting in minimal changes in the structure factor. This straightforward consideration is consistent with an analytical derivation in which the change in intensity is proportional to

$$\varepsilon \cdot (r - n_{BaTiO_3}/n) \tag{4}$$

valid for all m and l.[20,35]

In situ time-resolved x-ray microdiffraction allows the structural parameters of the repeating unit of the SL to be determined as a function of E.[20] Figure 5 shows the intensity of the $m=2$ $l=0$ reflection as a function of q_z at $E=0$ and at $E=1$ MV/cm. At $E=1$ MV/cm, the reflection appears at lower q_z than at $E=0$ due to the piezoelectric expansion of the lattice. Shaded regions of Fig. 5 show the range of q_z over which the intensity was integrated to be compared with the intensity of each satellite reflection calculated using kinematic diffraction simulations.

Figure 6 shows the experimental integrated intensities and the intensities obtained in the kinematic simulation for $l=-3$, -2, -1, 0, and 1 with $m=2$. Simulations are plotted in Fig. 6 as a function of ε for cases in which $r=0$, 1/3, and 1. We note that the change of simulated intensity is proportional to ε for the $r=0$, 1/3, and 1 cases, in agreement with the analytical approximation in expression (4). The experimental integrated intensity of each satellite corresponded to several hundred photons for each value of ε, with $l=-2$, -1, 0, and 1, leading to statistical uncertainty of approximately 5%. The $l=-3$ $m=2$ reflection had a lower intensity than the other $m=2$ reflections and as a result had an uncertainty of approximately 30%. The distribution of the large number of data points at $\varepsilon=0$ for each SL reflection illustrates the variation due to counting statistics.

The experimentally observed changes in the intensity as a function of ε in Fig. 6 are close to those predicted for the the $r=1/3$ case for all of the reflections for which the predicted change in the intensity is larger than the statistical uncertainty. For the $m=2$ $l=1$ reflection in Fig. 6(e), for example, the intensity is predicted to dramatically change with ε for $r=0$ and $r=1$ cases. At $\varepsilon=0.45\%$, the predicted intensities for the $r=0$ and $r=1$ cases are 0.6 and 2.2 times the $\varepsilon=0$ case, respectively, as shown in the inset of Fig. 6(e). The small experimentally observed variation in the intensity in Fig. 6(e) is in excellent agreement with $r=1/3$. Values of r were also evaluated in the same way using simulations of the satellite reflections of $2(BaTiO_3)/5(CaTiO_3)$ and $3(BaTiO_3)/4(CaTiO_3)$ SLs, compositions close to the measured period of the superlattice. In both cases, the values of r determined using the $m=2$ $l=1$ reflection, which has the strongest dependence of the intensity on r, are consistent with $r=n_{BaTiO_3}/n$, corresponding to equal strains in the $BaTiO_3$ and $CaTiO_3$ components.

A second set of SL reflection intensities was acquired for $m=1$. Figure 7 shows the experimentally measured intensity of the $l=-1$, 0, and 1 reflections with $m=1$ as a function of ε. For all of the $m=1$ SL reflections, the kinematic scattering model predicts that the change in intensity as a function of ε will be smaller than the experimental statistical uncertainty of 5%.

The simulation and experimental measurements were compared at the highest strain, $\varepsilon=0.45\%$, in order to extract values of r. Based on the model given in expression (4), the change in intensity at each value of ε is proportional to $(r-n_{BaTiO_3}/n)$, which we now use to obtain an estimate of r for each reflection. With $m=2$, this approach provides reliable estimates of r for all reflections except $m=2$ $l=0$, for which the dependence of the normalized intensities on r is weakest. For the $m=2$ $l=0$ reflection, the predicted intensity varies only from 1.02 to 0.95 as r covers the full range of its possible values, from 0 to 1. For the reflections at $m=1$, the predicted variation of the intensity with r is also small and our analysis yields a value of r only for the largest variation in intensity at $m=1$ $l=1$.

The values of r determined in our analysis are shown as solid symbols in Fig. 8. The values of r obtained from the $l=-2$, -1, and 1 reflections with $m=2$, for which the variation in predicted intensity with ε and r is sufficiently large, are close to the $r=1/3$ case. Other reflections, including $m=2$ $l=0$ and all the reflections at $m=1$, have variations in predicted intensity smaller than the statistical uncertainty of the measurement, and thus yield values of r that are unphysical and have large uncertainty. The solid and dotted lines in Fig. 8 indicate r for the cases in which the SL components have equal piezoelectric expansion $(r=1/3)$ or their bulk properties $(r=1)$, which would produce piezoelectric strain only in the $BaTiO_3$ component. The results in Fig. 8 show that the piezoelectric strain occurs in both $CaTiO_3$ and $BaTiO_3$ and that the bulk piezoelectric properties clearly pro-

TABLE I. Piezoelectric coefficients $e_{\alpha\beta}$ and $d_{\alpha\beta}$ for $2(BaTiO_3)/4(CaTiO_3)$ and $4(BaTiO_3)/2(CaTiO_3)$ SLs constrained to $P4mm$ symmetry. The coefficients for the $BaTiO_3$ film clamped to the $SrTiO_3$ substrate are also shown for comparison. The signs of $d_{\alpha\beta}$ depend on the definition of positive and negative stresses σ_α and were chosen to be consistent with the results of the experimental measurements, with tensile stresses considered as positive and compressive stresses as negative.

	$2(BaTiO_3)/4(CaTiO_3)$	$4(BaTiO_3)/2(CaTiO_3)$	$P4mm$ $BaTiO_3$
e_{33} (C/m^2)	8.5	6.3	4.4
d_{31} (pm/V)	−5.9	13.7	25.1
d_{33} (pm/V)	51.0	19.4	−10.8

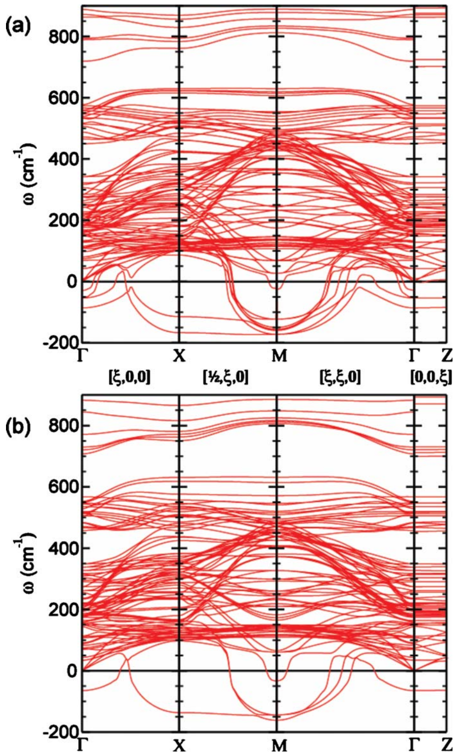

FIG. 11. (Color online) Calculated phonon dispersion curves of the (a) $2(\mathrm{BaTiO_3})/4(\mathrm{CaTiO_3})$ and (b) $4(\mathrm{BaTiO_3})/2(\mathrm{CaTiO_3})$ SLs along symmetric directions in the *P*4*mm* BZ. Imaginary frequencies associated with unstable phonon modes are plotted as negative numbers below the zero line.

vide a very poor match for the experimental results. One might expect that the piezoelectric coefficient of the $2(\mathrm{BaTiO_3})/4(\mathrm{CaTiO_3})$ SL would be as small as 1/3 of that of $\mathrm{BaTiO_3}$ thin film, based on the simple assumption that only $\mathrm{BaTiO_3}$ layers contribute to the overall piezoelectricity. The experimental results in Fig. 8 are instead consistent with a physical picture in which the $\mathrm{CaTiO_3}$ contributes to the piezoelectricity with a piezoelectric coefficient proportional to its remnant polarization,[14] and with the SL diffraction results discussed above and in Ref. 20. This picture is further supported by the theoretical results presented in the next section.

C. First-principles calculations of nonequilibrium properties

In order to understand the microscopic mechanism behind the piezoelectric response of the $2(\mathrm{BaTiO_3})/4(\mathrm{CaTiO_3})$ SL, we have conducted DFT-based simulations of this SL and of other structures with similar compositions. To probe the relationship between the changes in the SL layer composition and the resulting piezoelectric response, the calculations were performed for the experimentally characterized $2(\mathrm{BaTiO_3})/4(\mathrm{CaTiO_3})$ SL, a $4(\mathrm{BaTiO_3})/2(\mathrm{CaTiO_3})$ SL, and an epitaxially clamped $\mathrm{BaTiO_3}$ thin film.

After relaxation under the *P*4*mm* symmetry constraint, both SLs develop rumplings[36] in CaO layers due to large displacements of Ca ions. Both SLs also exhibit minimal layer-to-layer variation in the polarization, similar to the SLs reported in Ref. 37. The average polarization of the $2(\mathrm{BaTiO_3})/4(\mathrm{CaTiO_3})$ SL was computed to be $0.34\ \mathrm{C/m^2}$, only slightly lower than that of the $\mathrm{BaTiO_3}$ thin film clamped to the $\mathrm{SrTiO_3}$ substrate ($0.37\ \mathrm{C/m^2}$).[37]

In Fig. 9, layer rumplings in the $2(\mathrm{BaTiO_3})/4(\mathrm{CaTiO_3})$ SL are presented, calculated for $\varepsilon_3=0\%$ (solid line), as well as for ε_3 changing from -2% to 2% in steps of 0.5%. For comparison, the results of the same calculation for the clamped $\mathrm{BaTiO_3}$ film are also shown in the right panel of the same figure. At equal values of the imposed ε_3, the rumplings and, consequently, the layer polarizations in the SL are far larger than those of the film. Although one might expect the piezoelectric properties to be stronger in systems with a larger number of ferroelectric layers, calculations show the opposite trend: the SL with the largest fraction of $\mathrm{CaTiO_3}$ also has the highest predicted e_{33} and d_{33}.

The computed dependence of P_3 on ε_3, σ_1, and σ_3, for the experimentally probed $2(\mathrm{BaTiO_3})/4(\mathrm{CaTiO_3})$ SL and the $4(\mathrm{BaTiO_3})/2(\mathrm{CaTiO_3})$ SL are shown in Fig. 10 for values of ε_3 ranging from -2% to 2% in steps of 0.5%. Clamped piezoelectric coefficients e_{33}, d_{31}, and d_{33} were obtained from Fig. 10 using the linear relationships described in Sec. II B, and are presented in Table I. The calculated d_{33} value for the $2(\mathrm{BaTiO_3})/4(\mathrm{CaTiO_3})$ SL, 51 pm/V, is in excellent agreement with the experimental value of 54 pm/V.[20] Such closeness of the experimental and theoretical results suggests that when the measurements of the converse piezoelectric effect are made with high *E* the structure of the $2(\mathrm{BaTiO_3})/4(\mathrm{CaTiO_3})$ SL is close to the tetragonal *P*4*mm* symmetry as assumed in the DFT calculation.

We have also computationally evaluated the low-temperature stability of SLs constrained to the tetragonal *P*4*mm* symmetry under zero applied *E*. The SL phonon dispersions were calculated across the tetragonal BZ and checked for unstable branches. Computed phonon dispersions for the $2(\mathrm{BaTiO_3})/4(\mathrm{CaTiO_3})$ and $4(\mathrm{BaTiO_3})/2(\mathrm{CaTiO_3})$ SLs are shown in Figs. 11(a) and 11(b), respectively, with the imaginary frequencies of unstable phonon modes plotted below the zero line.

Table II summarizes the frequencies, symmetry labels, and the ionic distortion characters of the calculated unstable SL modes at the center and boundaries of the BZ. At $E=0$, numerous structural instabilities are present in the $2(\mathrm{BaTiO_3})/4(\mathrm{CaTiO_3})$ and $4(\mathrm{BaTiO_3})/2(\mathrm{CaTiO_3})$ SLs constrained to *P*4*mm* tetragonal symmetry. The doubly degenerate ferroelectric and antiferroelectric (AFE) instabilities at Γ correspond to rotations of layer polarizations away from the [001] direction in the $\mathrm{CaTiO_3}$ component layer. The antiferrodistortive (AFD) instabilities at the BZ boundary points correspond to rotations of the $\mathrm{TiO_6}$ octahedra either between two CaO monolayers or between CaO and BaO monolayers. Due to its larger volume fraction of $\mathrm{CaTiO_3}$, the $2(\mathrm{BaTiO_3})/4(\mathrm{CaTiO_3})$ SL exhibits a higher number of unstable phonon bands than the $4(\mathrm{BaTiO_3})/2(\mathrm{CaTiO_3})$ SL. For example, at the M point the $2(\mathrm{BaTiO_3})/4(\mathrm{CaTiO_3})$ SL has several antiferrodistortive rotational patterns, with the $\mathrm{TiO_6}$ octahedra in different $\mathrm{CaTiO_3}$ bilayers rotating either in-phase or out-of-phase around the [001] direction. The zone-boundary instabilities are much stronger than the zone-center instability for both SL compositions, indicating that the low-

TABLE II. Computed unstable phonon frequencies ω (cm^{-1}) in the 2(BaTiO$_3$)/4(CaTiO$_3$) and 4(BaTiO$_3$)/2(CaTiO$_3$) SLs constrained to *P*4*mm* symmetry at reciprocal space points Γ, X, and M. All structural instabilities are localized either in the CaTiO$_3$ component layer or at the interface between the CaTiO$_3$ and BaTiO$_3$. Instability characters, which are either ferroelectric (FE), antiferroelectric (AFE), or antiferrodistortive (AFD), are denoted in brackets after the symmetry labels, with subscripts indicating the sense of direction: axial (α) or planar ($\alpha\beta$) ionic motion for the FE and AFE modes, single (α) or an equivalent set (α,β) of rotational axes for the AFD modes [here $\alpha,\beta = x,y,z$].

Γ(0,0,0)		X(1/2,0,0)		M(1/2,1/2,0)	
Label	ω	Label	ω	Label	ω
4(BaTiO$_3$)/2(CaTiO$_3$)					
$E(\mathrm{FE}_{xy})$	65*i*	$A_1(\mathrm{AFD}_{x,y})$	137*i*	$B_1(\mathrm{AFD}_z)$	162*i*
				$E(\mathrm{AFD}_{x,y})$	144*i*
				$B_1(\mathrm{AFD}_z)$	34*i*
2(BaTiO$_3$)/4(CaTiO$_3$)					
$E(\mathrm{FE}_{xy})$	86*i*	$A_1(\mathrm{AFD}_{x,y})$	167*i*	$E(\mathrm{AFD}_{x,y})$	172*i*
$E(\mathrm{AFE}_{xy})$	54*i*	$A_1(\mathrm{AFD}_{x,y})$	115*i*	$B_1(\mathrm{AFD}_z)$	160*i*
				$B_1(\mathrm{AFD}_z)$	156*i*
				$B_1(\mathrm{AFD}_z)$	150*i*
				$E(\mathrm{AFD}_{x,y})$	123*i*
				$B_1(\mathrm{AFD}_z)$	24*i*

temperature ground state of the SL will include antiferrodistortive octahedral-cage rotations in the CaTiO$_3$ component layer.

The calculations thus predict that the tetragonal *P*4*mm* SL structure is unstable at low temperature and zero *E*. It is currently unclear whether the weaker in-plane ferroelectric instability in CaTiO$_3$ will be suppressed or promoted by freezing in of the octahedral-cage rotations and the work to elucidate this point is underway. Our investigation shows that there is a strong connection between the structural softness and piezoelectric properties in BaTiO$_3$/CaTiO$_3$ SLs. Further efforts will be necessary to fully understand the structural changes occurring in these systems under applied *E*.

IV. SUMMARY

We have used time-resolved x-ray microdiffraction and DFT calculations to evaluate the piezoelectric properties of each component of a model ferroelectric/dielectric SL. In the experimentally obtained diffraction patterns, superlattice reflections shift along the scattering wave vector in applied electric fields due to the piezoelectric distortion of 2(BaTiO$_3$)/4(CaTiO$_3$) superlattice. The integrated intensity of superlattice reflections shows a small change as a function of applied electric field, indicating that both the BaTiO$_3$ and CaTiO$_3$ components of each repeating unit have equal piezoelectric strains. The strain is consistent with the predicted remnant polarizations in both the bulk-ferroelectric BaTiO$_3$ and bulk-dielectric (nonpiezoelectric) CaTiO$_3$ components. The close link between polarization and piezoelectricity suggests that the sharing of the overall piezoelectric distortion we observe here will be a general feature of ferroelectric superlattices with other compositions in which the polarization is continuous. An assumption of tetragonal symmetry for the SL allows good agreement with the experimentally obtained piezoelectric coefficients. However, we predict a lower symmetry ground state for the SL at zero temperature due to a number of antiferrodistortive phonon instabilities in the CaTiO$_3$ component layer and at its interfaces. The coexistence of epitaxial strain, octahedral rotations, and interfaces between bulk-nonpolar and bulk-polar layers at the nanoscale allow this system to exhibit a rich range of phenomena and interesting opportunities for future development of superlattice materials with enhanced functional properties.

ACKNOWLEDGMENTS

P.G.E. acknowledges support by the U.S. Department of Energy through Contract No. DE-FG02-04ER46147 and by the U.S. National Science Foundation through Grant No. DMR-0705370. H.N.L. acknowledges support from the Materials Sciences and Engineering Division, U.S. Department of Energy through Contract No. DE-AC05-00OR22725. S.M.N. and the use of the Advanced Photon Source were supported by the U.S. Department of Energy under Contract No. DE-AC02-06CH11357.

[1] W. Tian, J. C. Jiang, X. Q. Pan, J. H. Haeni, Y. L. Li, L. Q. Chen, D. G. Schlom, J. B. Neaton, K. M. Rabe, and Q. X. Jia, Appl. Phys. Lett. **89**, 092905 (2006).

[2] M. B. Okatan, J. V. Mantese, and S. P. Alpay, Phys. Rev. B **79**, 174113 (2009).

[3] E. Bousquet, M. Dawber, N. Stucki, C. Lichtensteiger, P. Hermet, S. Gariglio, J. M. Triscone, and P. Ghosez, Nature (London) **452**, 732 (2008).

[4] K. Johnston, X. Huang, J. B. Neaton, and K. M. Rabe, Phys. Rev. B **71**, 100103 (2005).

[5] P. Zubko, N. Stucki, C. Lichtensteiger, and J. M. Triscone, Phys. Rev. Lett. **104**, 187601 (2010).

[6] S. S. A. Seo, H. N. Lee, and T. W. Noh, Thin Solid Films **486**, 94 (2005).

[7] H. N. Lee, H. M. Christen, M. F. Chrishlom, C. M. Rouleau, and D. H. Lowndes, Nature (London) **433**, 395 (2005).

[8] J. B. Neaton and K. M. Rabe, Appl. Phys. Lett. **82**, 1586 (2003).

[9] F. A. Urtiev, V. G. Kukhar, and N. A. Pertsev, Appl. Phys. Lett. **90**, 252910 (2007).

[10] L. Pintilie, I. Boerasu, and M. J. M. Gomes, J. Appl. Phys. **93**, 9961 (2003).

[11] A. L. Roytburd, S. Zhong, and S. P. Alpay, Appl. Phys. Lett. **87**, 092902 (2005).

[12] Y. L. Li, S. Y. Hu, D. Tenne, A. Soukiassian, D. G. Schlom, X. X. Xi, K. J. Choi, C. B. Eom, A. Saxena, T. Lookman, Q. X. Jia, and L. Q. Chen, Appl. Phys. Lett. **91**, 112914 (2007).

[13] A. Artemev, B. Geddes, J. Slutsker, and A. Roytburd, J. Appl. Phys. **103**, 074104 (2008).

[14] M. E. Lines and A. M. Glass, *Principles and Applications of Ferroelectrics and Related Materials* (Oxford University Press, New York, 1977).

[15] M. Dawber, N. Stucki, C. Lichtensteiger, S. Gariglio, P. Ghosez, and J. M. Triscone, Adv. Mater. **19**, 4153 (2007).

[16] J. F. Nye, *Physical Properties of Crystals* (Clarendon Press, Oxford, 1985).

[17] R. Ranjith, R. V. K. Mangalam, Ph. Boullay, A. David, M. B. Lepetit, U. Lüders, W. Prellier, A. Da Costa, A. Ferri, R. Desfeux, Gy. Vincze, Zs. Radi, and C. Aruta, Appl. Phys. Lett. **96**, 022902 (2010).

[18] R. Nath, S. Zhong, S. P. Alpay, B. D. Huey, and M. W. Cole, Appl. Phys. Lett. **92**, 012916 (2008).

[19] S. M. Nakhmanson, K. M. Rabe, and D. Vanderbilt, Phys. Rev. B **73**, 060101 (2006).

[20] J. Y. Jo, R. J. Sichel, H. N. Lee, S. M. Nakhmanson, E. M. Dufresne, and P. G. Evans, Phys. Rev. Lett. **104**, 207601 (2010).

[21] J. Y. Jo, R. J. Sichel, H. N. Lee, S. M. Nakhmanson, E. M. Dufresne, and P. G. Evans, MRS Symposia Proceedings, 1119E, 1199–F01–06 (2010).

[22] D.-H. Do, P. G. Evans, E. D. Isaacs, D. M. Kim, C. B. Eom, and E. M. Dufresne, Nature Mater. **3**, 365 (2004).

[23] D. H. Do, A. Grigoriev, D. M. Kim, C. B. Eom, P. G. Evans, and E. M. Dufresne, Integr. Ferroelectr. **101**, 174 (2008).

[24] P. Giannozzi *et al.*, J. Phys.: Condens. Matter **21**, 395502 (2009).

[25] D. Vanderbilt, Phys. Rev. B **41**, 7892 (1990).

[26] H. J. Monkhorst and J. D. Pack, Phys. Rev. B **13**, 5188 (1976).

[27] S. Baroni, S. de Gironcoli, A. Dal Corso, and P. Giannozzi, Rev. Mod. Phys. **73**, 515 (2001).

[28] R. D. King-Smith and D. Vanderbilt, Phys. Rev. B **47**, 1651 (1993).

[29] T. Furukawa, IEEE Trans. Electr. Insul. **24**, 375 (1989).

[30] I. Souza, J. Íñiguez, and D. Vanderbilt, Phys. Rev. Lett. **89**, 117602 (2002).

[31] E. E. Fullerton, I. K. Schuller, H. Vanderstraeten, and Y. Bruynseraede, Phys. Rev. B **45**, 9292 (1992).

[32] I. K. Schuller, M. Grimsditch, F. Chambers, G. Devane, H. Vanderstraeten, D. Neerinck, J. P. Locquet, and Y. Bruynseraede, Phys. Rev. Lett. **65**, 1235 (1990).

[33] J. Als-Nielsen and D. McMorrow, *Elements of Modern X-ray Physics* (Wiley, New York, 2001).

[34] B. L. Henke, E. M. Gullikson, and J. C. Davis, At. Data Nucl. Data Tables **54**, 181 (1993).

[35] R. M. Fleming, D. B. McWhan, A. C. Gossard, W. Wiegmann, and R. A. Logan, J. Appl. Phys. **51**, 357 (1980).

[36] C. Bungaro and K. M. Rabe, Phys. Rev. B **71**, 035420 (2005).

[37] S. M. Nakhmanson, K. M. Rabe, and D. Vanderbilt, Appl. Phys. Lett. **87**, 102906 (2005).